J. Jpn. Soc. Microgravity Appl. Vol. 28 No. 2 2011 (S51–S56)

8th Japan-China-Korea Workshop on Microgravity Sciences
for Asian Microgravity Pre-Symposium

Phase Selection in the Undercooled Melts of $RMnO_3$ (R=rare earth) Using Containerless Solidification Technique

Vijaya KUMAR [1*], Kazuhiko KURIBAYASHI [1,2], Jianding YU [1], Masashi KANEKO [1], Takehiko ISHIKAWA [3] and Shinichi YODA [1]

Abstract

The low oxygen partial pressure Po_2 of an ambient atmosphere is considerably effective for phase selection in the $RMnO_3$ system, since the Mn ion changes its valence states depending on Po_2. Containerless solidification of the undercooled $RMnO_3$ melt was carried out to study phase formation behavior under precisely controlled Po_2. The orthorhombic and hexagonal $RMnO_3$ phases were solidified from an undercooled melt at $Po_2=10^5$ Pa. X-ray diffraction patterns and cross-sectioned microstructure revealed the existence of orthorhombic and hexagonal $RMnO_3$. Thermodynamic stabilities were studied at various temperatures. The oxygen deficiencies in the as-solidified samples were calculated through annealing at 10^5 Pa using TG-DTA. These results suggest that the containerless solidification is one of the most suitable methods for phase equilibrium study under controlled Po_2.

1. Introduction

In the $RMnO_3$ system, orthorhombic perovskite structure with a space group of *Pbnm* is thermodynamically stable for the rare earth elements having larger ionic radius (R=La-Dy), whereas the hexagonal structure with a space group of $P6_3cm$ is stable for the smaller ionic radius elements (R=Ho-Lu and Y)[1-4]. The hexagonal compounds with $P6_3cm$ shows lower crystallographic symmetry i.e., noncentrosymmetric structure due to slightly distorted oxygen packing. A direct consequence of the appearance of such a noncentrosymmetric structure was the possibility of ferroelectricity[5,6] with spontaneous polarization along the hexagonal axis. The crystal structure of the orthorhombic (*Pbnm*) and hexagonal ($P6_3cm$) $RMnO_3$ is shown in **Fig.1**. Recently, rare-earth manganites have attracted great interest due to the multiferroic property, i.e., the coexistence of ferroelectricity and magnetism in one compound [7-9].

Goldschmidt [10] discussed the stability of the perovskite structure using the tolerance factor:

$$t = \frac{R_R + R_O}{\sqrt{2}\left(R_{Mn} + R_O\right)} \quad (1)$$

Here, R_R and R_{Mn} are ionic radii of rare earth and manganese, respectively, and R_O is the ionic radius of oxygen. In the $RMnO_3$ system, the perovskite structure becomes relatively unstable as the ionic radius decreases from La (0.1032 nm) to Lu (0.0861 nm). After systematic investigation, Goldschmidt summarized that the perovskite structure is stable at $t > 0.8$ and contrary unstable at $t < 0.8$. In the R-Fe-O system, although the ionic radii of Mn^{3+} and Fe^{3+} (0.0645 nm for 6 coordination) [11] are nearly the same, hexagonal $P6_3cm$ was formed metastably for the rare-earth elements having small ionic radius (R=Gd to Lu) [12-14]. This clearly indicates that Po_2 plays an important role in the formation of metastable phases due to the change of valence from Fe^{3+} to Fe^{2+} under reduced oxygen atmosphere.[15] Therefore, there is also a possibility that the same kind of phenomenon may occur even in the R-Mn-O system due to the reduction of Mn^{3+} to Mn^{2+} under reduced Po_2. Therefore, study of the effect of Po_2 in the R-Mn-O systems under non-equilibrium system is of great importance.

Containerless processing with levitation technique allows for cooling of molten samples several hundred degrees below the liquidus temperature until spontaneous crystallization or recalescence occurs. A Levitation technique can supply a new method for phase equilibrium study, because the existence of a liquid phase makes easy to achieve phase equilibria. However, there have been a very few reports on the formation of rare earth manganites of orthorhombic and multiferroic hexagonal compounds from an undercooled $RMnO_3$ melt through containerlss solidification.

In the present study, containerless solidification of $RMnO_3$ from an undercooled melt under reduced Po_2 was attempted using an aerodynamic levitation technique to elucidate the effect of the rare earth species on phase selection. We will show the

1 ISS Science Project Office, Institute of Space and Astronautical Science (ISAS), Japan Aerospace Exploration Agency (JAXA), 3-1-1 Yoshinodai, Sagamihara, Kanagawa 252-5210, Japan
2 Department of Materials Science and Engineering, Shibaura Institute of Technology, Toyosu, Koto-ku, Tokyo 135-8548, Japan
3. ISS Science Project Office, Japan Aerospace Exploration Agency (JAXA), 2-1-1 Sengen, Tsukuba, Ibaraki, 305-8505, Japan

(* Corresponding Author E-mail: vijaya.kumar@jaxa.jp)

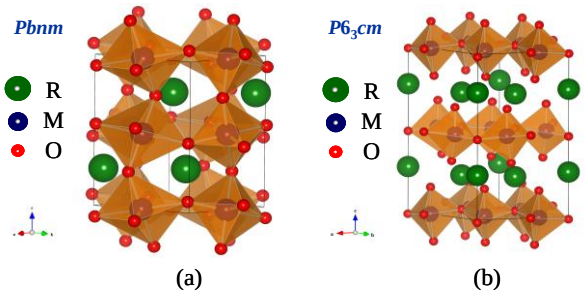

Fig. 1 Crystal structure of (a) orthorhombic $RMnO_3$ with a space group of *Pbnm* and (b) hexagonal $RMnO_3$ with a space group of $P6_3cm$.

possibility for direct formation of orthorhombic and hexagonal $RMnO_3$ from undercooled melts.

2. Experimental Procedure

2.1 Sample Preparation

The R_2O_3 and MnO_2 powders were weighed in the $RMnO_3$ composition and completely melted by a CO_2 laser into spherical samples on a water-cooled copper hearth. The typical sample diameter and mass were ~2 mm and 20-25 mg, respectively. Recently, a rather simple apparatus for rapid solidification in which an aerodynamic levitator (ADL) combined with a ZrO_2 oxygen sensor was designed in order to deeply undercool the melt under a precisely controlled oxygen partial pressure [15]. A spherical $RMnO_3$ sample was levitated by an ADL using O_2 gas at a flow rate of ~ 600 ml/min and completely melted by a CO_2 laser. The flow rate of the levitation gas was controlled using a mass flow controller (CR-300, Kofloc, Kyoto, Japan). Two-color pyrometer was used to monitor the surface temperature of the levitated droplet at a sampling rate of 100 Hz with central wavelengths of 0.9 and 1.55 μm and spot diameter of 1 mm. Then, the droplet was cooled by turning off the CO_2 laser. Meanwhile, an In-situ observation of the solidification behavior on the sample surface was monitored using a high-speed video (HSV) camera at a sampling rate of 1 kHz with a spatial resolution of 256×240 pixels. The detailed description of the experimental setup is given in elsewhere [12]. The effect of rare-earth species on the phase selection, perovskite or hexagonal phase was studied for the undercooled $RMnO_3$ melt by varying the rare-earth elements from La to Lu. The as-solidified sample was annealed in the same atmosphere of 10^5 Pa to study the phase stabilities at various temperatures.

2.2 Characterization

The surface morphologies and cross-sectional microstructures of the as-solidified and annealed samples were observed by scanning electron microscopy (SEM), and chemical compositions of the phases were analyzed by energy-dispersive spectroscopy (EDS). The constituent phases were identified using X-ray diffractometry (XRD) over a 2θ range of 5–80°. The differential thermal analysis (DTA) and thermogravimetric analysis (TGA) measurements were carried out to study the phase stability of the constituent phases in the temperature range from room temperature to 1673 K.

3. Results

3.1 Cooling Curve

The effects of oxygen partial pressure on the formation of orthorhombic and hexagonal phases were studied from the undercooled $RMnO_3$ melts at P_{O_2}=1x10^5 Pa**.** The recalescence phenomenon was observed visually in all samples due to the release of latent heat during crystallization of the solid phase, and the increase in temperature was measured using two-color pyrometer. The nucleation (T_N) and post-recalescence (T_P) temperatures as a function of ionic radius of rare-earth elements were shown in **Fig. 2**. Inserted figure shows the typical cooling curve of the as-solidified sample. The T_N and T_P decreased with decreasing ionic radius of the rare earth elements from La (T_N=1980 K and T_P=2220 K) to Dy (T_N=1530 K and T_P=1890 K) and gradually increased with further decreasing of ionic radius from Ho (T_N=1540 K and T_P=1910 K K) to Lu (T_N=1730 K and T_P=1960 K).

3.2 Phase Identification

In order to identify the phase constituents, rapidly solidified $RMnO_3$ samples were characterized using XRD. The XRD

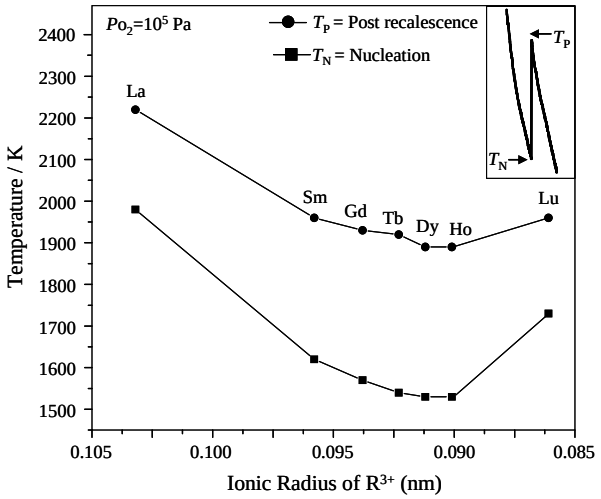

Fig. 2 Nucleation (T_N) and post-recalescence (T_P) temperatures of the rapidly solidified $RMnO_3$ samples at 1x10^5 Pa recorded using a two-color pyrometer at a sampling rate of 100 Hz.

patterns of the as-solidified samples were recorded using monochromatic radiation with a wavelength of 0.154 nm for Cu$K\alpha$ and are shown in **Fig. 3**. The orthorhombic $RMnO_3$ perovskite (*o*-$RMnO_3$) with a space group of *Pbnm* was identified in the large ionic radius elements such as from La to Tb (**Fig. 3**(a)), whereas both *o*-$RMnO_3$ and hexagonal $RMnO_3$ (*h*-$RMnO_3$) phases were solidified only in the $DyMnO_3$ (**Fig. 3**(b)) sample solidified at 10^5 Pa. On the other hand, only *h*-$RMnO_3$ with a space group of $P6_3cm$ was identified for the small ionic radius elements from Ho to Lu and Y (**Fig.3**(c)). This indicates that the $DyMnO_3$ is located at the boundary between the hexagonal and the perovskite phases.

3.3 *In-situ* Observation

3.3.1 $LaMnO_3$

In-situ observation of the solidification process was recorded using a color HSV camera. The typical solidification behaviors of the rapidly solidified $LaMnO_3$ samples are shown in **Fig.4**. The frames are taken at a time interval of 0.001 s, and elapsed time indicated in each image was set at 0 s for one frame before the nucleation. In the $LaMnO_3$ sample processed at 10^5 Pa (**Fig. 4**(a)), solid phase nucleated from the undercooled melt and solidification process completed after 5 ms with showing a single recalescence, i.e., the phase formed was retained at room temperature without any phase transformation. The same kind of solidification path was also observed at 10^3 Pa (**Fig. 4**(b)). The

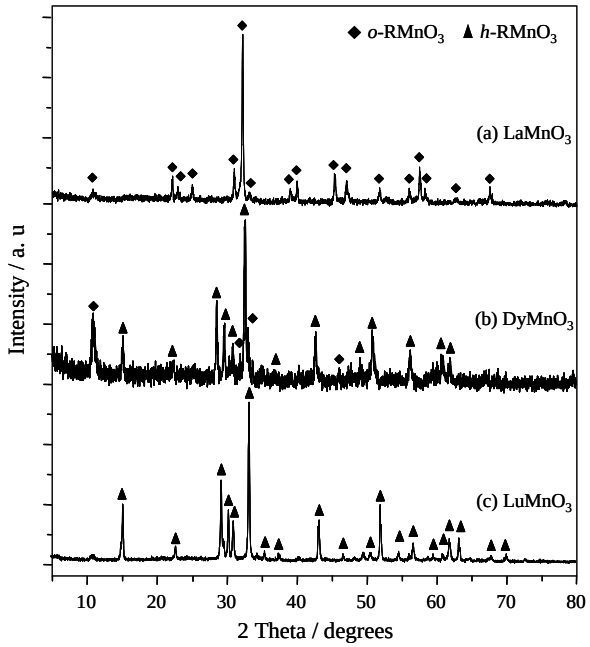

Fig. 3 X-ray diffraction patterns of the $RMnO_3$ samples solidified at 10^5 Pa. The filled diamond and triangle symbols represent *o*-$RMnO_3$ and *h*-$RMnO_3$ respectively.

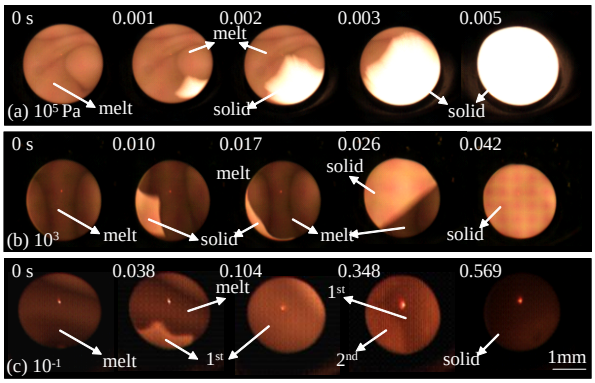

Fig. 4 Solidification behavior of the $LaMnO_3$ samples processed at (a) $Po_2 = 10^5$ Pa, (b) 10^3 Pa and (c) 10^{-1} Pa. The solidification process was captured by color HSV camera at a sampling rate of 1 kHz.

dark and bright regions of the photograph represent the undercooled melt and the growing solid, respectively. The liquid and solid phases can be distinguished by difference in emissivity of both phases. The solid-liquid interface is clearly indicated by the large difference in brightness between the solid and liquid. On the hand, two-step recalescence, i.e., solid-solid phase transformation was observed at 10^{-1} Pa (**Fig.4**(c)). At the first recalescence, a disk-like solid phase was initiated in the undercooled melt and solidification completed at 0.104 s. After the completion of first recalescence, second recalescence was initiated from the solid at 0.348 s and completed at 0.569 s. In all the samples, increase in the solidification time was observed from 0.005 s to 0.569 s with decreasing Po_2 from 10^5 to 10^{-1} Pa, respectively.

3.3.2 $LuMnO_3$

An *in-situ* observation of the solidification process of the $LuMnO_3$ is shown in **Fig. 5**. In the sample solidified at 10^5 Pa, single recalescence was observed, as shown in **Fig. 5**(a). On the other hand, two-step recalescence was observed in the samples processed at 10^3 and 10^{-1} Pa (**Figs. 5**(b) and **6**(c)). The solidification time was decreased from 0.134 s to 0.105 s with decreasing Po_2 to 10^{-1} Pa. This might be due to the decrease of volume fraction of *h*-$LuMnO_3$ phase with forming Lu_2O_3 and Mn-rich phases.

3.4 Surface Morphology

The surface morphologies of the as-solidified $LaMnO_3$ samples taken using SEM are shown in **Fig. 6**. All the samples shown in **Figs 6**(a), **6**(b) and **6**(c) show the spherical shape with dendritic structures. The surface morphologies gradually changed from dendritic to faceted planes with decreasing Po_2 down to 10^{-1} Pa (see **Figs. 6**(a1), (b1), and (c1). The XRD

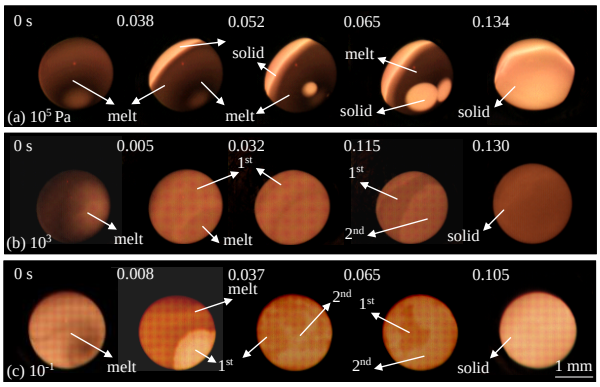

Fig. 5 Solidification behavior of the $LuMnO_3$ samples processed at (a) $Po_2 = 10^5$ Pa, (b) 10^3 and (c) 10^{-1} Pa.

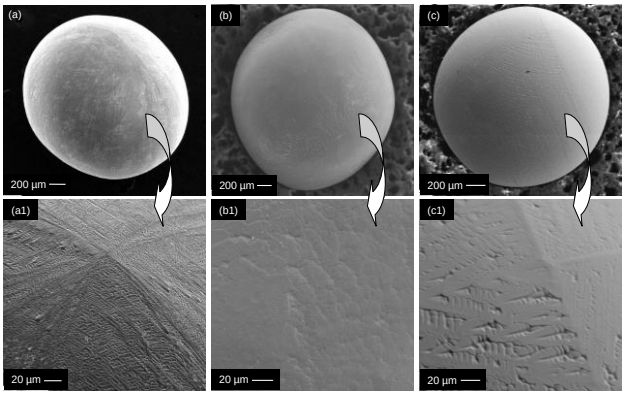

Fig. 6 Surface morphologies of the as-solidified $LaMnO_3$ samples observed using scanning electron microscopy (SEM). (a) 10^5, (b) 10^3, and (c) 10^{-1}. The magnified images (a1) 10^5, (b1) 10^3, and (c1) 10^{-1} Pa, clearly shows the dendritic and faceted planes.

results in **Fig. 3** confirmed the existence of *o*-$LaMnO_3$ phase. This clearly indicates that the dendritic structure is due to the existence of *o*-$LaMnO_3$.

3.5 Microstructure

Figure 7 shows the cross-sectioned images of the $RMnO_3$ samples observed using SEM. The microstructure of the $LaMnO_3$ sample consisted of *o*-$LaMnO_3$ and La-rich phases. As shown in **Fig. 7**(a), the composition ratio of the La-rich phase was not identified due to very fine grain size, but this phase would be La_2O_3 due to evaporation of small amount of Mn_2O_3. The volume fraction of the La-rich phase was very small; hence the peak patterns were not detected by XRD. The XRD results of $DyMnO_3$ (**Fig. 3**) showed the existence of both orthorhombic and hexagonal phases. However, it was difficult to distinguish the orthorhombic and hexagonal phases in **Fig. 7**(b). Since the average atomic number is the same for both phases, there is almost no contrast difference between perovskite and hexagonal phases. A small volume fraction of dark and light phases were identified and these phases might be Mn_2O_3 and Dy_2O_3, respectively. Moreover, it was difficult to separate the phases because of the small grain size. The volume fraction of the *h*-$RMnO_3$ increased with decreasing ionic radius and *h*-$RMnO_3$ was formed for Ho and Lu (see **Figs. 7**(c) and **7**(d)). The chemical compositions of the as-solidified phases were also confirmed by energy-dispersive spectroscopy analysis.

4 Discussion

4.1 Thermodynamic Stability

According to the XRD and SEM results, orthorhombic phase was not selected but hexagonal phase predominated with decreasing ionic radius from La to Lu. The change in the crystal structure from orthorhombic to hexagonal was identified in the $DyMnO_3$ sample. In order to elucidate the phase stabilities, as-solidified samples were annealed at various temperatures using TG-DTA apparatus at a heating rate of 20 K/min. The annealing Po_2 condition was the same as that for solidification. As-solidified $LaMnO_3$ samples were heated up to 1673 K for 1 h and cooled down to room temperature. As shown in **Fig. 8**, the XRD patterns of the as-solidified $LaMnO_3$ sample confirmed the existence of the *o*-$LaMnO_3$ phase. The peak intensities of the *o*-$LaMnO_3$ phase completely transformed into cubic $LaMnO_3$ (*c*-$LaMnO_3$) at 1673 K. This confirmed that the *c*-$LaMnO_3$ is stable at 1673 K at 10^5 Pa.

We also studied the thermodynamic stabilities of the other $RMnO_3$ samples. The peak intensities of the *h*-$HoMnO_3$ and h-$DyMnO_3$ decreased with increasing annealing temperature and only orthorhombic phase was formed after annealing at 1673 K. This clearly indicates that *h*-$DyMnO_3$ phase formed metastably along with the stable *o*-$DyMnO_3$. This suggests that single phase of *h*-$DyMnO_3$ will be obtained as a metastable phase with Po_2 lower than 10^5 Pa. Moreover, no phase transformation was observed in the $YMnO_3$ and $LuMnO_3$ i.e. as-solidified hexagonal phase retained even after annealing at 1673 K. These results clearly suggest that the as-solidified *h*-$HoMnO_3$ and *h*-$DyMnO_3$ are thermodynamically metastable, whereas the *h*-$YMnO_3$ and *h*-$LuMnO_3$ are stable hexagonal phases.

4.2 Tolerance Factor

As mentioned in introduction, Goldschmidt [10] discussed the stability of the perovskite structure using the tolerance factor "t" (Eq. (1)) and suggested that the perovskite structures become unstable as the ionic radii of the rare-earth elements decreases with increasing atomic number from La to Lu. Since the ionic radius of Mn^{2+} (0.0830 nm for 6 coordination) is larger than that of Mn^{3+} (0.064 nm for 6 coordination) [11], partial substitution of Mn^{2+} in the perovskite structure results in a smaller tolerance

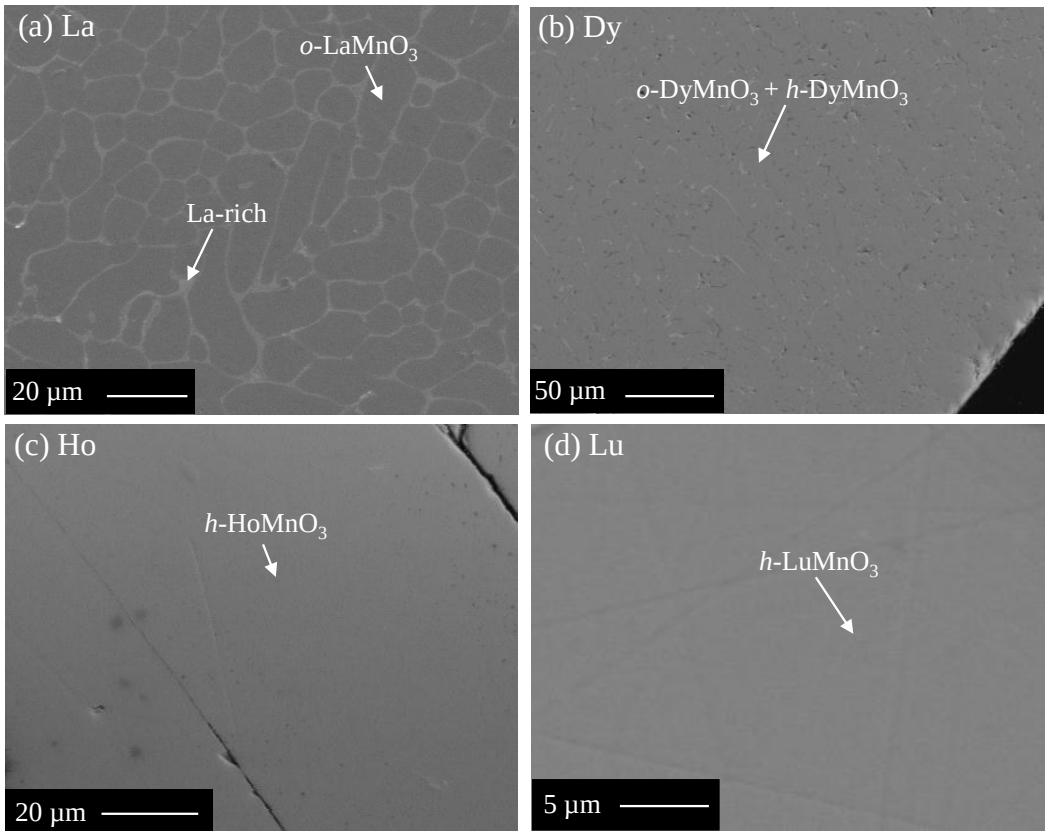

Fig. 7 Cross sectioned micrographs of the $RMnO_3$ samples solidified at 10^5 Pa. (a) $LaMnO_3$), (b) $DyMnO_3$, (c) $HoMnO_3$ and (d) $LuMnO_3$

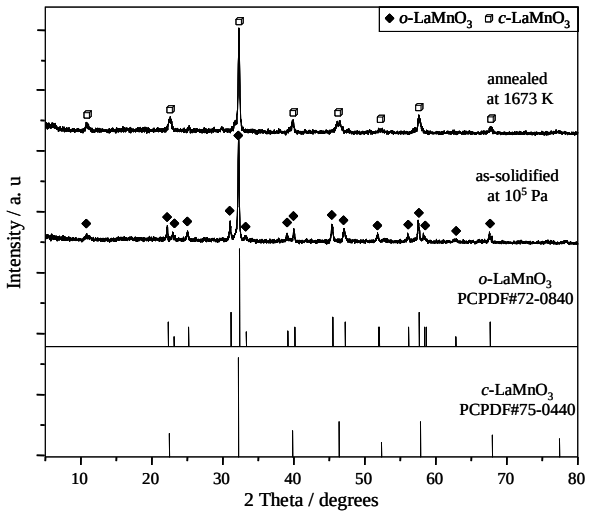

Fig. 8 X-ray diffraction patterns of as-solidified and annealed $LaMnO_3$ samples. The diamond and cubic symbols represent *o*-$LaMnO_3$ and *c*-$LaMnO_3$ phases, respectively.

factor. Here, in order to calculate the tolerance factor, average ionic radius of oxygen and Mn ions were calculated for $R^{3+}Mn^{3+}_{(1-2x)}Mn^{2+}_{(2x)}{}^{O2-}_{(3-x)}$ compositions and represented in **Fig. 9**. Experimentally obtained results were compared with those of the theoretically calculated results. This result indicates that the oxygen deficiencies in the $RMnO_3$ sample leads to the decrease in tolerance factor. This result clearly suggests that the orthorhombic and hexagonal phases formed due to the decrease of "tolerance factor".

4.3 Undercooling

The containerless solidification process provides large undercooling prior to nucleation which often leads to the formation of stable/metastable phases. Hence, undercooling, which exceeds the difference between the melting point of the stable phase and that of the metastable phase, generates a driving force for solidification of the metastable phase from a melt [16,17]. The temperature difference between T_N and T_P is usually called as undercooling level (ΔT) (see the inserted Fig. in **Fig 10**). As shown in **Fig. 10**, an undercooling level varied with varying rare earth ionic radius. The undercooling level seems to increase gradually as the ionic radius of the rare-earth elements increases with forming *h*-$RMnO_3$ phase (**Fig. 3**) and decreased with further increase of ion radius form Tb to La with forming *o*-$RMnO_3$. The maximum undercooling of 380±10 K was achieved for $TbMnO_3$, whereas, the minimum undercooling of 230±10 K was achieved in the $LaMnO_3$. The driving force for

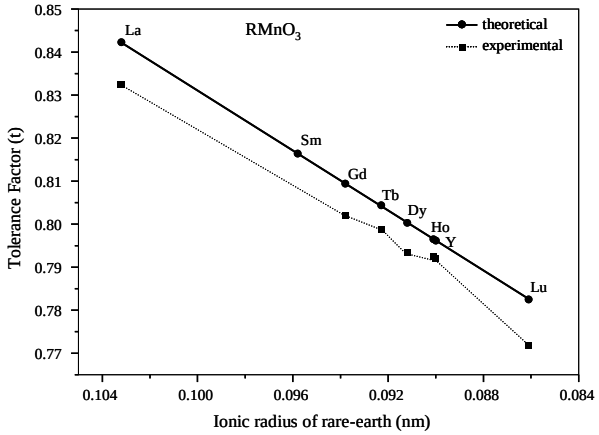

Fig. 9 Relationship between the tolerance factor and an ionic radius of rare-earth elements.

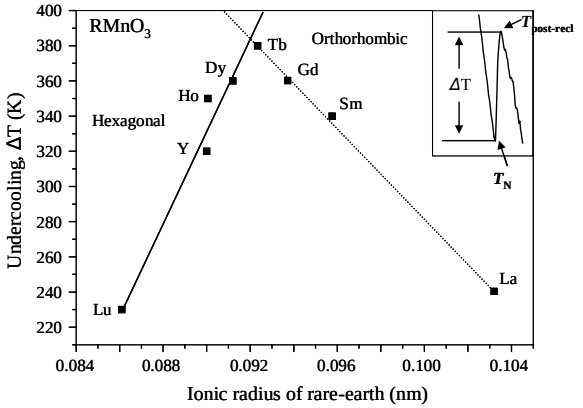

Fig. 10 Undercooling levels of the $RMnO_3$ samples recorded using a two color pyrometer.

the solidification of hexagonal and orthorhombic intersects at a particular point where hexagonal phase may solidify in Tb. This indicates that in order to obtain the hexagonal and orthorhombic phases, it is necessary to achieve an undercooling over 380 K for the formation of hexagonal and orthorhombic phases for the large (Tb to La) and small ionic radius elements (Dy to Lu), respectively. This suggests that undercooling level would play an important role during phase selection from an undercooled melt under controlled oxygen partial pressure.

5. Conclusions

The containerless solidification of an undercooled $RMnO_3$ melt, where the undercooling level can be treated as one of the major experimental parameter, was carried out to explore the phase formation behavior of orthorhombic and multiferroic hexagonal $RMnO_3$ under controlled Po_2. The phase transformation from orthorhombic to hexagonal was observed with decreasing ionic radius from La to Lu. Moreover, both orthorhombic and hexagonal $RMnO_3$ were obtained in the $DyMnO_3$. The samples annealed at 1673 K at 10^5 Pa showed the stable perovskite $RMnO_3$ phase, suggesting that as-solidified hexagonal $HoMnO_3$ and $DyMnO_3$ are thermodynamically metastable at 10^5 Pa. TGA results suggested that the tolerance factor decreases with increasing oxygen deficiency in the as-solidified sample. In this study, phases were formed from the liquid state where the reaction rate is very fast to form homogeneous compounds and the solubility of oxygen in the melt is larger than that of the solid. Therefore, a levitation technique is a good tool for phase equilibrium study.

Acknowledgements

The authors wish to acknowledge Prof. T. Hibiya, Keio University, Japan, for the encouragement and valuable discussions during experiment. This work was financially supported by a Grant-in-Aid for Scientific Research from The Ministry of Education, Culture, Sports, Science and Technology, Japan.

References

1) H. L. Yakel, W. C. Koehler, E. F. Bertaut and E. F. Forrat: Acta. Cryst., **16** (1963) 957.
2) I. K. Jeong, N. Hur and Th. Proffen: J. Appl. Cryst., **40** (2007) 730.
3) A. A. Bossak, C. Dubourdieu, J.P. Senateur, Y. Gorbenko, and A. R. Kaul: Crys. Eng., **5** (2002) 355.
4) T. Katsufuji, M. Masaki, A. Machida, M. Moritomo, K. Kato, E. Nishiobori, M. Takata, M. Sakata, K. Ohoyama, K. Kitazawa, and H. Takagi: Phy. Rev. B, **66** (2002) 134434 (1).
5) I. E. Graboy, A. A. Bosak, O. Yu. Gorbenko, A. R. Kaul, C. Dubourdieu, J. P. Senateur, V. L. Svetchnikov, and H. W. Zandbergen: Chem. Mater., **15** (2003) 2632.
6) M. Isobe, N. Kimizuka, M. Nakamura, and T. Mohri: Acta Cryst. C, **47** (1991) 423.
7) T. Kimura, T. Goto, H. Ishizaka, T. Arima and Y. Tokura: Nature, **426** (2003) 55.
8) J. S. Zhou, J. B. Goodenough, J. M. Gallardo, E. Moran, M. A. A. Franco, and R. Caudillo: Phys Rev. B, **74** (2006) 014422 (1).
9) S. W. Cheong and M. Mostovoy: Nat. Mat. **6** (2007) 13.
10) V. M. Goldschmidt: Geochemische Verteilungsgesetze der Elemente VII. (Die Gesetze der Krystallochemie. Math -Naturv. K1. Oslo, Norway, 1926, 97.
11) R. D. Shannon: Acta Cryst. A, **32** (1976) 751-67.
12) M. S. Vijaya Kumar, K. Nagashio, T. Hibiya, and K. Kuribayashi: J. Am. Ceram. Soc., **91** (2008) 806.
13) K. Nagashio and K. Kuribayashi: J. Am. Ceram. Soc., **85** (2002) 2550
14) A. A. Bossak, I. E. Graboy, O. Y. Gorbenko, and A. R. Kaul: Chem. Mater., **16** (2004) 1751.
15) M. S. Vijaya Kumar, K. Kuribayashi, and K. Kitazono: J. Am. Ceram. Soc., **92** (2009) 903.
16) D. M. Herlach: Mater. Sci Eng. R. **12** 272 (1994) 177.
17) K. Kuribayashi, K. Nagashio, K. Niwata, M. S. Vijaya Kumar, and T. Hibiya: Mater Sci Eng A, **449-451** (2007) 675.

(Received 21 Sept. 2010; Accepted 8 Aug. 2011)